PHYSICAL REVIEW B VOLUME 37, NUMBER 16 1 JUNE 1988

Excited-state-absorption and laser parameters of V^{2+} in MgF_2 and $KMgF_3$

R. Moncorgé and T. Benyattou
Laboratoire de Physico-Chimie des Matériaux Luminescents, Université de Lyon I,
43 boulevard du 11 Novembre 1918, 69622 Villeurbanne, France

(Received 3 June 1987)

We report here absolute excited-state-absorption (ESA) measurements in the V^{2+}-doped vibronic laser systems MgF_2 and $KMgF_3$. The results show no detrimental ESA in the wavelength region of the possible laser pump sources around 500 nm. ESA in the wavelength domain of infrared laser emission is important only in the case of MgF_2:V^{2+}. A discussion is made concerning to what extent these results could have been predicted. The already reported laser tunability of MgF_2:V^{2+} between 1.07 and 1.15 μm is then verified and the laser system $KMgF_3$:V^{2+} is found tunable between ~0.95 and 1.15 μm.

I. INTRODUCTION

Since the pioneer work[1] of Johnson and Guggenheim in 1967, who demonstrated lasing action with broadband visible excitation in MgF_2:V^{2+}, few other experiments have be done or communicated about V^{2+} as an active ion in other laser hosts: a few results have appeared about tunable laser operation in MgF_2:V^{2+} and $KMgF_3$:V^{2+} in various internal reports and conferences[2,3] and a full article has recently come out about the laser potentiality of a variety of V^{2+}-doped halide crystals.[4]

The V^{2+} ion is isoelectronic with Cr^{3+}; consequently the energy levels and the optical properties of V^{2+} in crystals should be very similar to those of Cr^{3+}, the ones are known to give good lasing properties in an increasing number of new systems. Like with Cr^{3+}, the same distinction is possible between high-field systems, such as MgO:V^{2+}, and low-field systems, such as MgF_2:V^{2+}, the former being characterized, as in ruby, by a $^2E \rightarrow {}^4A_{2g}$ narrow-band fluorescence, the latter by a broadband $^4T_{2g} \rightarrow {}^4A_{2g}$ fluorescence.

Also, the emission bands that we get with V^{2+} in low-field systems extend between around 0.9 and 1.3 μm, i.e., in a wavelength domain which is not presently covered by any other vibronic laser systems based on transition metal ions such as Cr^{3+} as well as Ni^{2+} or Co^{2+}, and this wavelength domain appears of a particular interest for a number of applications (fusion driver, semiconductor spectroscopy, etc.). Among the reasons which make this research area so much underdeveloped, we note the following: (i) the crystal growth of the V^{2+} doped systems is not easy; (ii) the number of low-field systems which can incorporate the V^{2+} divalent ions is very much restricted compared with the series of the Ge and Ga garnets used with Cr^{3+}; (iii) the V^{2+} ion is characterized by a large ionic radius (≈0.88 Å); thus it is subjected to stronger ion-lattice interactions which result in broader optical bands but also in stronger nonradiative transitions; (iv) the V^{2+}-doped systems are subjected to excited-state absorption in the wavelength domain of optical pumping (reabsorption) as well as in the domain of emission which seems more detrimental for laser operation than in the case of Cr^{3+}.

As a matter of fact, in the present work, we have tried to clarify these last two points by analyzing the optical properties of the two laser systems MgF_2:V^{2+} and $KMgF_3$:V^{2+}. It follows a similar study which was dedicated to Ni^{2+} in MgF_2 and MgO.[5] A part of the paper, Sec. II, recall and complete our knowledge of the general optical properties (ground-state absorption, emission, fluorescence lifetime, and quantum efficiency) of MgF_2:V^{2+} and $KMgF_3$:V^{2+}. A subsequent part, Sec. III, is then devoted to the description of the experimental techniques and the procedure used to get our excited-state absorption data. In Sec. IV we analyze these results on the basis of the configuration curve model. In the end, an attempt at generalization is made.

II. GENERAL OPTICAL PROPERTIES

The low-temperature ground-state absorption (GSA) characteristics of V^{2+} in MgF_2 and $KMgF_3$ have been already reported.[6] However, because it is important in the following we complete these data by reporting in Figs. 1 and 2 the GSA spectra recorded at room temperature.

As in the case of Cr^{3+} in low-field systems, the spectra are made of three broadbands which are attributed, in the order of increasing energies, to the well-known spin-allowed vibronic transitions noted, in the cubic field approximation, $^4A_2 \rightarrow {}^4T_2$, $^4A_2 \rightarrow {}^4T_{1a}$, and $^4A_2 \rightarrow {}^4T_{1b}$. By comparing the spectra, we find out that when the systems are warmed up above ~100 K, the bands shift to the red, by about 300 cm^{-1} at room temperature, and the $^4T_2$ no-phonon lines which are clearly observed at low temperature at ~10 100 and 10 930 cm^{-1} in MgF_2:V^{2+} and $KMgF_3$:V^{2+}, respectively, completely disappear. The absorption spectra of $KMgF_3$:V^{2+} do not show any polarization effect because the V^{2+} ion occupies sites having O_h symmetry. In MgF_2, the site group of the V^{2+} ion has D_{2h} orthorhombic symmetry and the bands are α, σ and/or π polarized. As asserted before the $^4T_2$ optical band is mainly magnetic dipole (π coincides with axial α, but π and σ are not very different), which means that its

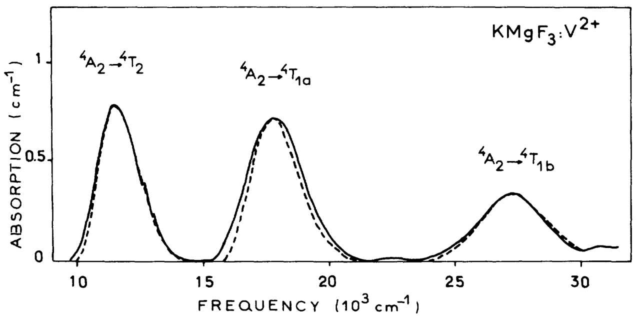

FIG. 1. Room-temperature absorption spectrum of KMgF$_3$ containing $\simeq 8.5\times10^{19}$ ions V^{2+}/cm^3. Solid line: experimental spectrum; dashed line: theoretical treatment using the CC model and SF theory (see the text).

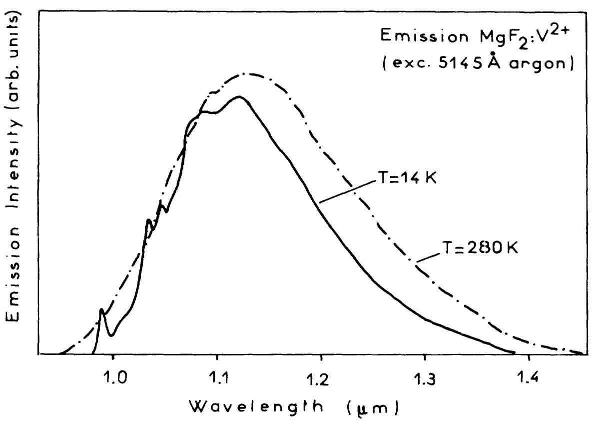

FIG. 3. Infrared emission spectra of MgF$_2$:V^{2+}.

intensity is not very sensitive to temperature, while the $^4T_{1a}$ and $^4T_{1b}$ optical bands are electric dipole (σ agrees with α) induced by odd-parity vibrations.

Consequently, in KMgF$_3$:V^{2+}, only spin-orbit coupling can split the various optical bands. However, the bands do not show enough structures to make a serious analysis of the band shapes in terms of individual spin-orbit components. Moreover, the spin-orbit splitting can be strongly modified by the Jahn-Teller effect.[6] As a consequence, we will ignore it in the following developments. In the case of MgF$_2$:V^{2+} we can assign the various σ and π polarized features of the spectrum in terms of orbital components since the D_{2h} distortion is likely stronger than the spin-orbit interaction.[7] In a field of D_{2h} symmetry the ground state $^4A_2$ transforms like $^4B_1$, and according to the calculations of Ref. 7, the state $^4T_2$ split into three components $^4B_2$, $^4B_1$, ^4A, the state $^4T_{1a}$ into $^4B_1$, $^4B_2$, $^4B_3$, and the state $^4T_{1b}$ into $^4B_2$, $^4B_3$, $^4B_1$, in order of increasing energies. The order of these levels can be further checked in the case of the $^4T_1$ states if one observes the fact that the polarization properties of the electric dipole $^4T_1$ optical bands depend on the symmetry of the odd-parity vibrations of the system (B_{1u}, B_{2u}, and B_{3u} for the D_{2h} local site symmetry).

The sharp structures which can be distinguished even at room temperature on the high-energy side of the $^4T_2$ absorption band are related to GSA transitions to the doublet states noted ^2E and $^2T_{1a}$,[8] and the bumps which may be observed around 23 000 cm^{-1} to GSA transitions to the doublet states noted $^2A_1$, $^2T_{2b}$, and $^2T_{1c}$. The infrared emission spectra of V^{2+} in MgF$_2$ and KMgF$_3$ are reported in Figs. 3 and 4 at low and high temperatures knowing that, except for some smoothing, the spectra remain unchanged up to ~100 K. Above this temperature the bands shift to the red as in absorption, by some 200 cm^{-1} in MgF$_2$:V^{2+} against 500 cm^{-1} in KMgF$_3$:V^{2+}, and the bandwidths increase by a factor ~1.4. Their temperature dependences are just those which are reflected by their respective fluorescence lifetimes as it is shown in Fig. 5. These dependences are very much different: the infrared fluorescence lifetime in MgF$_2$:V^{2+} is much more sensitive to temperature than it is in KMgF$_3$:V^{2+}. Analogous behaviors can be observed

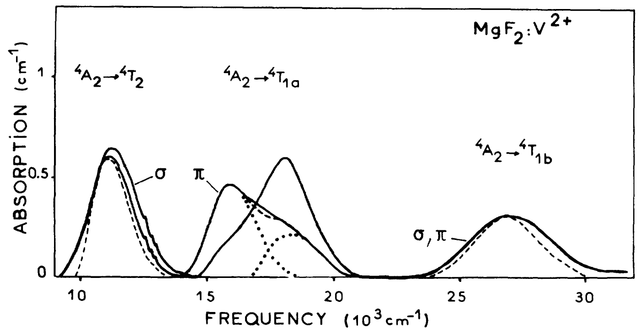

FIG. 2. Room-temperature absorption spectrum of MgF$_2$ containing $\simeq 3.5\times10^{19}$ ions V^{2+}/cm^3 in π and/or σ polarizations. Solid line: experimental spectrum; dashed line: theoretical treatment using the CC model and SF theory (see the text).

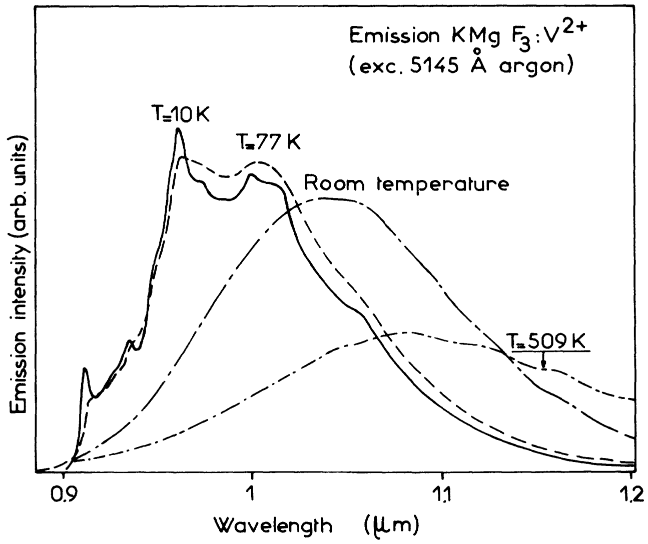

FIG. 4. Infrared emission of KMgF$_3$:V^{2+}.

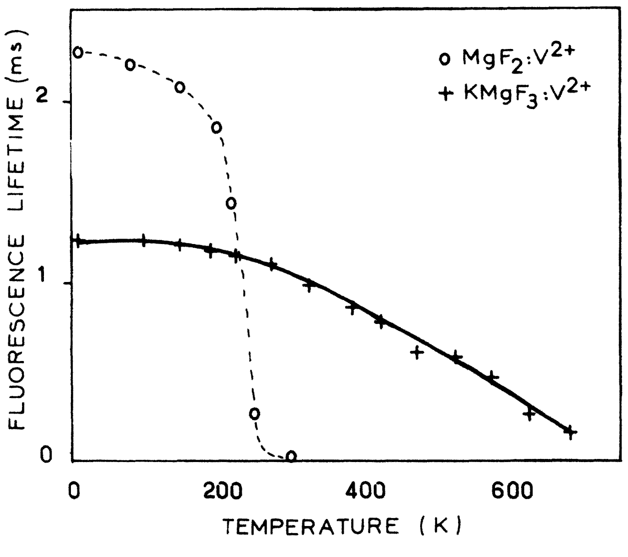

FIG. 5. Infrared emission lifetime vs temperature in $KMgF_3:V^{2+}$ (solid line: SF model) and $MgF_2:V^{2+}$,

in the case of Ni^{2+} in MgF_2 and MgO.[9,10] This temperature behavior can be made more quantitative by using the theory of Struck and Fonger[11] (SF) based on the well-known model of the configuration curves (CC). In this model a computer program is used to fit the temperature dependence of the ir fluorescence lifetime to the expression:

$$\frac{1}{\tau}=\frac{1}{\tau_0}+N_u U_{P_u} ,$$

where τ_0 is the radiative lifetime, N_u a constant of the model, and U_{P_u} the summed thermal Franck-Condon (FC) weighting factor defined in the SF theory.

In the case of $KMgF_3:V^{2+}$, the thermal expansion of the lattice induces such an important band shift at $T \gtrsim 270$ K that three sets of parameters were necessary to fit the data.

Set 1: for $T \lesssim 270$ K, $S=2.45$, $P_u=20$.
Set 2: for 270 K $\lesssim T \lesssim 500$ K, $S=2.25$, $P_u=19$.
Set 3: for $500 \lesssim T \lesssim 680$ K, $S=1.98$, $P_u=18$.

All sets have the common values $\tau_0=\tau(T=0)=1.2$ ms, $\hbar\omega=550$ cm^{-1}, and $N_u=1\times10^{13}s^{-1}$. The product $P_u\hbar\omega$ is the energy of the zero-phonon transition. The decreasing values of P_u, the number of 550 cm^{-1} phonons which are necessary to overcome the excited-state→ground-state energy gap, is consistent with the above-mentioned band shifts. As to the so-called Franck-Condon (FC) offset S, which measures the shift of the excited-state and ground-state parabola in the CC model in units of $\hbar\omega$, its temperature variation also agrees with the thermal expansion of the lattice: S is related to the electron-phonon coupling thus to the distances between the impurity ion and its nearest neighbors. The value $\hbar\omega=550$ cm^{-1} give the best fit to the data; it is consistent with a maximum of the phonon density of states in this material.[12]

In $MgF_2:V^{2+}$ the temperature variation of the fluorescence lifetime tends to indicate interacting phonons of lower energy, of the order of 250 cm^{-1}, as in the case of $MgF_2:Ni^{2+}$. However, 250 cm^{-1} phonons[9] lead to unrealistic results if one uses, as above, the SF analysis; more than 40 phonons would be necessary to overcome the energy gap and an extraordinarily large N_u constant should be postulated. This discrepancy may arise from the local site symmetry; in $MgF_2:V^{2+}$ the D_{2h} orthorhombic site symmetry allows more phonon modes to be coupled, and it makes the nonradiative transitions to the ground state much more probable than it does in the cubic system $KMgF_3:V^{2+}$. Also, the V^{2+} ion is so large that interactions with ligands beyond the first nearest neighbors should be non-negligible. Indeed, as in Cr^{3+}-doped low-field systems,[13] thermal quenching of V^{2+} fluorescences is strongly host dependent.[4]

Nevertheless, use was made of the data to establish the single configuration-coordinate diagrams reported in Figs. 6 and 7. These diagrams assume that all the ion-lattice interactions can be approximated by the coupling to a single frequency phonon of a_{1g} symmetry which means potential curves with the same curvature. The positions of the potential minima are determined by diagonalizing the well-known Tanabe-Sugano (TS) matrices and choosing the values of the usual crystal field and Racah parameters Dq, B, and C in order to get the best

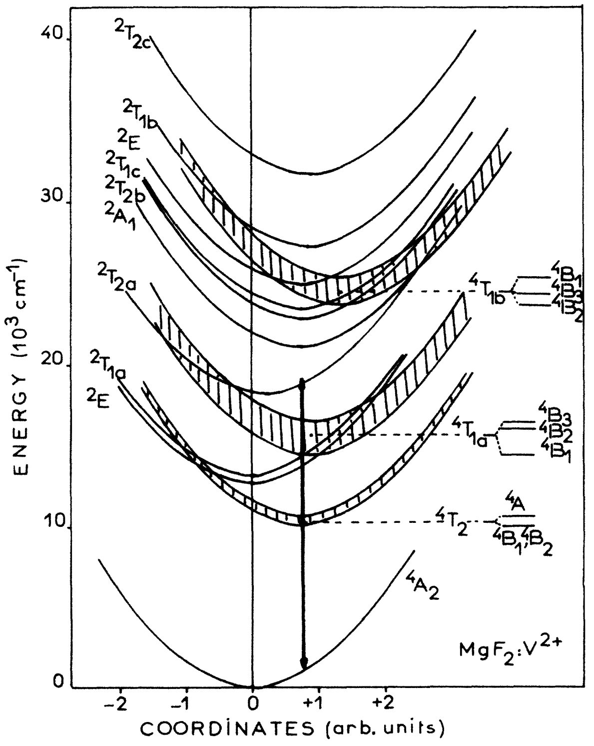

FIG. 6. Configuration curve diagram for $MgF_2:V^{2+}$ (upward and downward arrows: energy of the emitted photons).

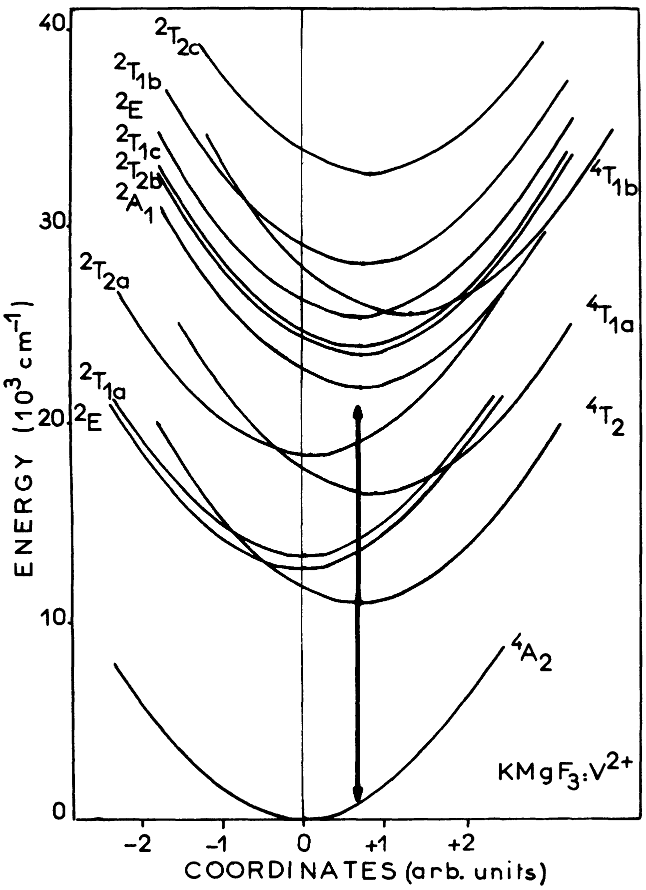

FIG. 7. Configuration curve diagram for KMgF$_3$:V^{2+} (upward and downward arrows: energy of the emitted photons).

agreement with the zero-phonon energies of levels $^4T_2$, ^2E, $^2T_{1a}$, and $^2T_{2a}$.

We find, assuming $C \simeq 4.5\ B$,

$$Dq = 1035\ \text{cm}^{-1} \text{ and } B = 615\ \text{cm}^{-1} \text{ in } \text{MgF}_2\text{:V}^{2+}\ ,$$

$$Dq = 1091\ \text{cm}^{-1} \text{ and } B = 615\ \text{cm}^{-1} \text{ in } \text{KMgF}_3\text{:V}^{2+}\ .$$

The infrared absorption and emission data (band positions, band profiles, temperature behaviors) are used to determine the shift between the ground-state and the first excited-state parabola in terms of the dimensionless FC offset parameter a in the space of the coordinates. a is proportional to the displacement of the V^{2+}-ligand internuclear distance; it is related to the FC offset S defined before by $a = 2\sqrt{S}$. The other potential curves are placed according to the slope of variation of the various electronic term energies for small variations $\delta(Dq)$ of the crystal-field parameter, each energy curve being shifted by its own quantity a. These calculations are made under the approximation that $\delta(Dq)$ is proportional to the displacement of the V^{2+}-ligand distance while B and C are independent of it. In the case of MgF$_2$:V^{2+} the positioning of the levels has been obtained by including the up and down displacements induced by the orthorhombic crystal-field splittings of the cubic terms as given in Ref. 6. The results of these calculations are compared to the experimental data in Tables I and II (Calc. 1). The single configuration coordinate mode gives a rather good overall description of the ground-state-absorption and infrared emission data.

Only the $^4A_2 \rightarrow {}^4T_{1b}$ absorption band is found at higher energy than expected, which is merely due to the simplicity of the calculations. Refinements have been obtained by fitting the broadband spectra with the line-shape functions W_p (S, $\hbar\omega$, T) defined in the theory of

TABLE I. Observed and calculated energies of the optical transition in MgF$_2$:V^{2+} at low and high temperatures (parentheses are used for the room-temperature positions) following diagonalization of the TS matrices with $Dq = 1035$ cm^{-1} and $B = 615$ cm^{-1} (Calc. 1) and subsequent refinements using the SF line-shape functions W_p with $\hbar\omega = 550$ cm^{-1} (Calc. 2).

Optical transitions	Zero-phonon energy (cm^{-1}) Obs.	Calc. 1	Calc. 2	Vibronic sideband energy (cm^{-1}) Obs.	Calc. 1	Calc. 2	Calculated $S\ \hbar\omega$ (cm^{-1})
$^4A_2 \rightarrow {}^4T_2$	10 100	10 150	(10 400)	11 500	11 050	(11 200)	$\simeq 900$
		10 750		(11 300)	11 650		
$^4A_2 \rightarrow {}^2E$	12 700	12 660					$\simeq 0$
$^4A_2 \rightarrow {}^2T_{1a}$	1 3400	13 230					$\simeq 0$
$^4A_2 \rightarrow {}^2T_{2a}$	18 200	18 260					$\simeq 60$
$^4A_2 \rightarrow {}^4T_{1a}$		14 500	(14 850)	16 300(π)	15 800	(15 900)	$\simeq 1\,300$
		16 100		(16 000)			
		16 500		18 350(σ)	17 400	(18 400)	
				(18 200)	17 800		
$^4A_2 \rightarrow {}^4T_{1b}$		23 700	(24 900)		26 500	(27 200)	$\simeq 2\,800$
		24 400		27 300	27 200		
		25 400		(27 300)	28 200		

TABLE II. Observed and calculated energies of the optical transition in $KMgF_3{:}V^{2+}$ at low and high temperatures (parentheses for the room-temperature positions) following diagonalization of the TS matrices with $Dq=1091$ cm^{-1} and $B=615$ cm^{-1} (Calc. 1) and subsequent refinements using the SF line-shape functions W_p with $\hbar\omega=550$ cm^{-1} (Calc. 2).

Optical transitions	Zero-phonon energy (cm^{-1}) Obs.	Calc. 1	Calc. 2	Vibronic sideband energy (cm^{-1}) Obs.	Calc. 1	Calc. 2	Calculated $S\hbar\omega$ (cm^{-1})
$^4A_2\to{}^4T_2$	10 910	10 910	(10 700)	11 800 (11 500)	11 850	(11 500)	$\simeq$1 000
$^4A_2\to{}^2E$	12 670	12 680					$\simeq$0
$^4A_2\to{}^2T_{1a}$	13 350	13 250					$\simeq$0
$^4A_2\to{}^2T_{2a}$	18 430	18 400					$\simeq$67
$^4A_2\to{}^4T_{1a}$		16 410	(16 500)	18 200 (17 850)	17 870	(17 800)	$\simeq$1 460
$A_2\to{}^4T_{1b}$		25 540	(24 300)	27 500 (27 300)	28 500	(27 300)	$\simeq$3 170

Struck and Fonger.[11] The results are shown in Figs. 1 and 2: the shapes and the widths of the broadbands are almost perfectly reproduced. They have been obtained by using the $S\hbar\omega$ values found in the above TS treatment (see Tables I and II) and by choosing the most suitable $\hbar\omega$ value. It is found that $\hbar\omega\simeq 550$ cm^{-1} in $KMgF_3{:}V^{2+}$ as well as in $MgF_2{:}V^{2+}$. In the calculations of the vibronic line-shape functions the energies of the zero-phonon origins are known only relatively. Their absolute values are merely obtained by fitting the experimental data with these band profiles. These adjustments lead to the new sets of zero-phonon and vibronic sideband energies reported in Tables I and II (Calc. 2).

From a laser point of view, the 5145 Å radiation of a CW argon laser seems a particularly suitable pump source. It is clear that $KMgF_3{:}V^{2+}$ appears as a good candidate for room temperature tunable laser operation in a wavelength domain likely going from $\sim$0.95 to 1.15 μm while in $MgF_2{:}V^{2+}$ tunable laser action is expected at cryogenic temperatures such as liquid-nitrogen (LN) temperature between $\sim$1.05 and 1.2 μm. As a matter of fact, it has been already reported in the past[2,3] room-temperature gain measurements at 1.065 μm in $KMgF_3{:}V^{2+}$ and tunable laser operation between $\sim$1.07 and 1.15 μm at LN temperature in $MgF_2{:}V^{2+}$. It is now one of the purposes of the following section to know more about the real laser possibilities of these systems

III. EXCITED-STATE-ABSORPTION MEASUREMENTS

Measurements of ESA cross sections in the wavelength regions of possible pump sources as well as of laser emis-

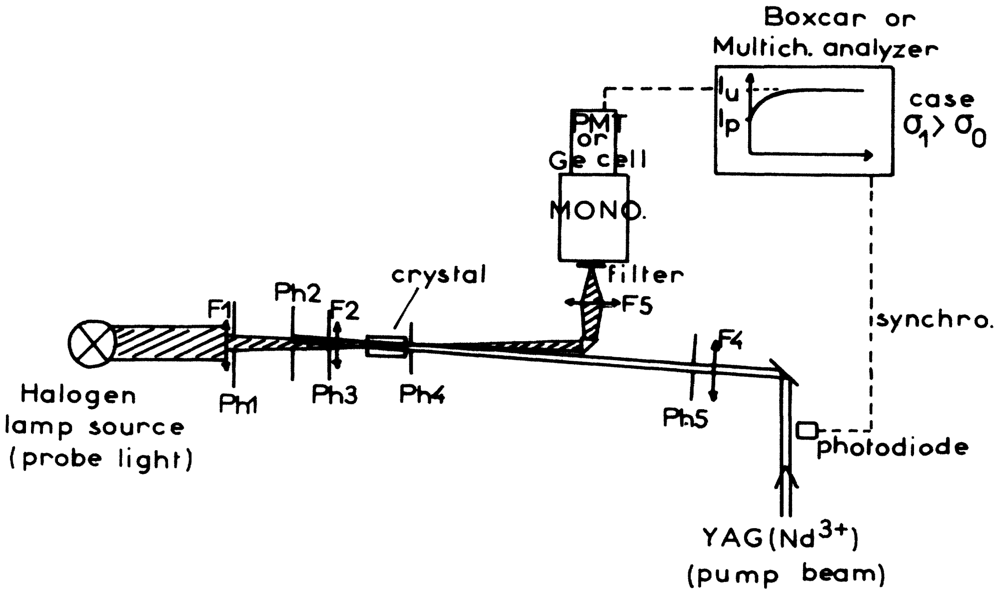

FIG. 8. Excited-state-absorption setup. PH means pinhole and F means lens.

sion give a quantitative point of view on the laser potentiality of these broadband vibronic systems. They give us a definitive insight on their laser efficiency and effective range of tunability. The method used to get our ESA spectra and cross sections is very similar to the one used by Andrews *et al.*,[14] for example, in the case of the Cr^{3+}-doped systems GSGG, GSAG, and K_2 $NaSCF_6$. It consists in the measurement of the change in the transmission (absorption) of a weak probe beam when it passes through a pumped and unpumped crystal. As shown in Fig. 8, the pump and probe beam are made collinear. The pump light is provided here by the 5320-Å radiation—which means $^4T_{1a}$ level excitation—of a second-harmonic pulsed YAG:Nd^{3+} laser from Quantel, and the probe light by an Oriel high power 1-kW halogen lamp source. The transmitted light is analyzed by appropriate monochromators and detected by a fast-response EMI 9808 photomultiplier or an ADC model 403 HS germanium photodiode cooled to LN temperature depending on the investigated visible or infrared wavelength domain. The signals are fed either into an IN90 intertechnique multichannel analyzer or a NIC 320 digital oscilloscope from Nicolet instruments connected to a PAR model 115 amplifier. The adjustments of the lenses and the pinholes are made because the pump beam overlaps the probe beam in the crystal and also to avoid the stray light. The spectra are recorded by scanning the monochromator in the wavelength region of interest and by registering and analyzing the transient signal after each selected wavelength. The method bears upon the measurement of the change in absorption coefficient noted $\Delta\alpha$, with

$$\Delta\alpha=\ln(I_u/I_p)/L=(\sigma_1-\sigma_0)N_1 ,$$

where I_p and I_u stand for the transmitted probe light intensity when the crystal is pumped and unpumped, respectively, L is the light path length in the sample, σ_0 and σ_1 the ground-state and the excited-state-absorption cross sections, and N_1 the excited-state population density. Since N_1 is produced by a pulsed pump excitation, it behaves like

$$N_1=N_1(0)\exp\left[-\frac{t}{\tau_1}\right] ,$$

where τ_1 is the rate of relaxation of the absorbing excited state. Thus being based on measurements of transient signals decaying with the same time constant as the lifetime of the absorbing level, this method ensures which

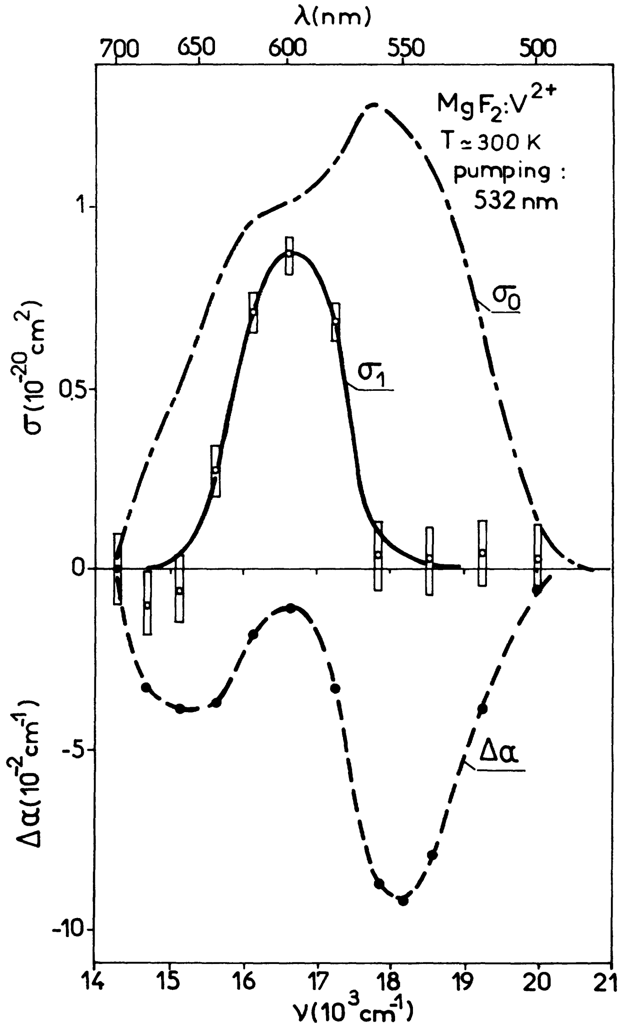

FIG. 9. $^4A_2\rightarrow{}^4T_{1a}$ GSA cross section σ_0, measured excited-state difference spectrum $\Delta\alpha$ and ESA cross section σ_1 in MgF_2:V^{2+}.

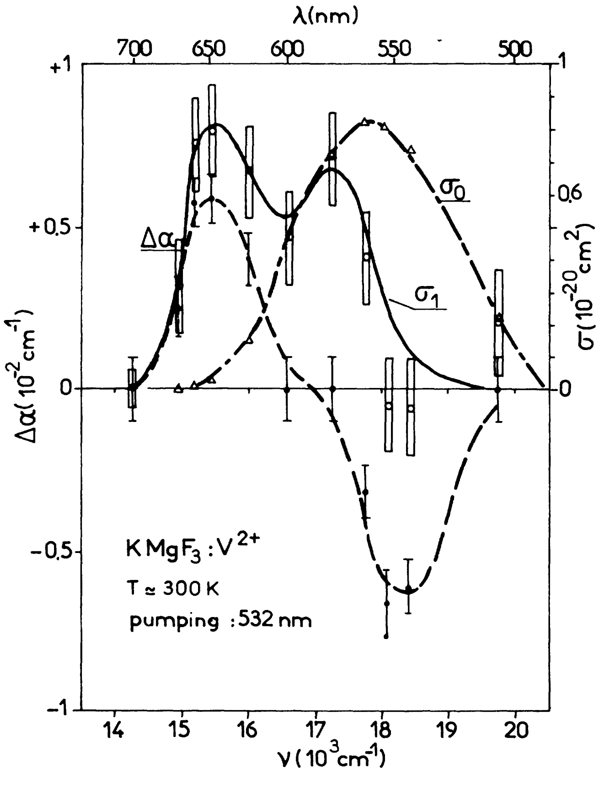

FIG. 10. $^4A_2\rightarrow{}^4T_{1a}$ GSA cross section σ_0, measured excited-state difference spectrum $\Delta\alpha$ and ESA cross section σ_1 in $KMgF_3$:V^{2+}.

excited state is actually absorbing; indeed, recent results in Ni^{2+}-doped compounds[5] have proved that, depending on the excitation wavelength, excited-state absorption may well occur in a state different from the lowest infrared emitting state, thus with a different excited state absorption dynamics.

Both σ_0 and N_1 must be known to extract σ_1. $\sigma_0 = k_0 N$, where k_0 is the GSA coefficient and N is the total active ion concentration. N_1 is estimated both from the excitation pump intensity and the pumped volume and, when it is possible, from the spectra at the wavelengths where $\sigma_1 = 0$, i.e., $\Delta\alpha = -\sigma_0 N_1$.

The excited-state difference spectra ($\Delta\alpha$ versus wavelength or energy) of MgF_2:V^{2+} and $KMgF_3$:V^{2+} obtained in the visible region are reported in Figs. 9 and 10 along with the GSA and the resulting ESA spectra σ_0 and σ_1 in the same domain. The transient signals all decay with the same time constant as the infrared fluorescences thus ensuring that the $^4T_2$ metastable state is the only absorbing excited state in each of these materials. The spectra have been recorded at room temperature because in the case of $KMgF_3$:V^{2+} it is likely at this temperature that the system should lase, but also because it is more convenient when high-excitation pump powers are needed.

The MgF_2:V^{2+} sample was a 1.9-cm long high optical quality single crystal doped with $\sim 3.5 \times 10^{19}$ V^{2+} ions/cm^3. The $KMgF_3$:V^{2+} single crystal was a 0.75-cm long sample doped with $\sim 8.5 \times 10^{19}$ V^{2+} ions/cm^3.

The probe light was unpolarized so that the data for MgF_2:V^{2+}, $\Delta\alpha$, σ_1 as well as σ_0, must be interpreted accordingly. In $KMgF_3$:V^{2+}, about 7 mJ of the 5320 Å pump radiation were absorbed, then producing an estimated excited-state population density $N_1 \simeq (7.6 \pm 0.5) \times 10^{17}$ ions/cm^3 which corresponds to an excitation ratio $N_1/N \simeq 1\%$. In MgF_2:V^{2+} more than 29 mJ were absorbed in the crystal in order to produce an estimated excited-state population density $N_1 \simeq (7 \pm 0.5) \times 10^{18}$ ions/cm^3 corresponding now to an excitation ratio $N_1/N \simeq 20\%$.

The $\Delta\alpha$ spectrum of MgF_2:V^{2+} (Fig. 9) is entirely negative which means that the σ_1 ESA cross section is always weaker than σ_0. The σ_1 spectrum is made of only one broadband peaking at about 6000 Å ($\sim 16\,600$ cm^{-1}). One notes that there is no measurable excited-state absorption at the wavelengths of the possible pump sources mentioned before, i.e., at 5145 and 5320 Å, which is very favorable for laser operation.

The excited-state difference spectrum $\Delta\alpha$ in $KMgF_3$:V^{2+} (Fig. 10) goes through zero at about 5900 Å ($\sim 17\,000$ cm^{-1}) and the resulting σ_1 ESA spectrum is made of two broadbands with peaks at about 5800 Å ($\sim 17\,250$ cm^{-1}) and 6500 Å ($\sim 15\,400$ cm^{-1}). Here again the σ_1 and σ_0 peak cross sections are of the same order of magnitude and there is no important excited-state absorption at 5145 or 5320 Å.

Measurements not shown in Figs. 9 and 10 reveal that no other appreciable ESA is present up to at least 30 000 cm^{-1} (3300 Å), this short wavelength limit being imposed by the lamp source and the detector.

Attempts were also made to measure ESA in the infrared and more particularly in the wavelength region of laser emission. Unfortunately we only have succeeded in the case of $KMgF_3$:V^{2+}, and yet for wavelengths longer than 1.38 μm (~ 7250 cm^{-1}) because of the experimental limitation arising from the spontaneous emission of the sample which overwhelms the halogen probe beam in the fluorescence region. The data are shown in Fig. 11 with other spectral curves which will be discussed in the next section.

No workable data could have been derived in the case of MgF_2:V^{2+} because of the experimental limitation men-

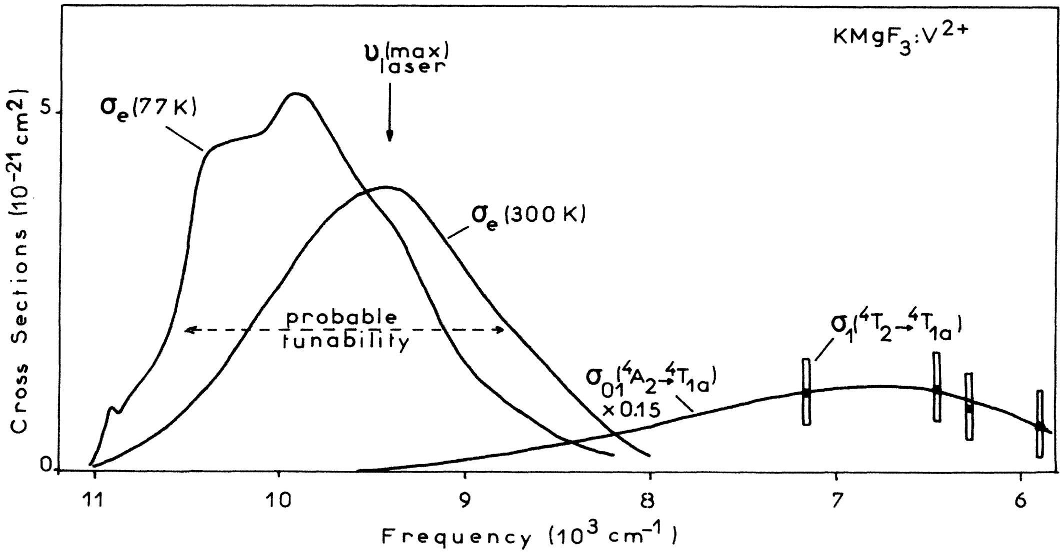

FIG. 11. Stimulated emission cross section σ_e, $^4A_2 \rightarrow {}^4T_{1a}$ GSA spectrum shifted by the energy of the $^4T_2$ zero-phonon transition σ_{01} and measured cross section σ_1 in $KMgF_3$:V^{2+}.

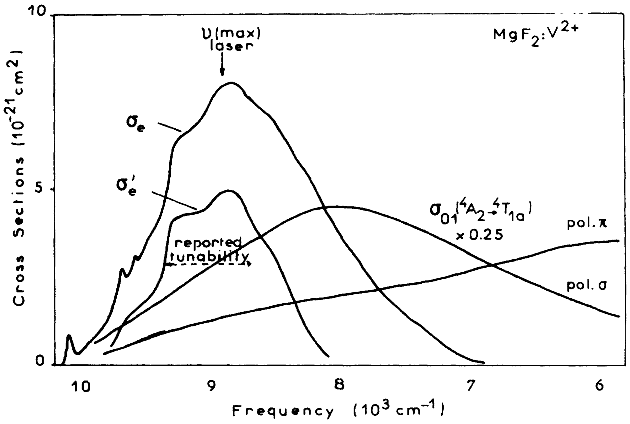

FIG. 12. Stimulated emission cross section σ_e, ${}^4A_2 \rightarrow {}^4T_{1a}$ GSA spectrum shifted by the energy of the ${}^4T_2$ zero-phonon transition σ_{01} and estimated net gain cross section σ'_e in MgF$_2$:V^{2+}.

tioned above but also and mainly because the short-lived ESA signals were strongly perturbed by the noise induced by the laser pump electronics on the germanium detector (see Fig. 12).

IV. DISCUSSION OF THE RESULTS

It is clear that the positions and the dynamics of the ESA broadbands observed in the visible region identify them as the spin-allowed ${}^4T_2 \rightarrow {}^4T_{1b}$ optical transition. As to the data points obtained in KMgF$_3$:V^{2+} in the infrared domain they must be attributed to the other spin-allowed ESA optical transition ${}^4T_2 \rightarrow {}^4T_{1a}$. No trace of spin-forbidden ESA transition is observed.

With this in mind we report in Figs. 13 and 14 the band shapes and the positions of the ESA transitions from the metastable state ${}^4T_2$ to the states ${}^4T_{1a}$ and ${}^4T_{1b}$ (1) by assuming, as in Ref. 1, these band shapes to be identical to that for the transitions from the ground state to ${}^4T_{1a}$ and ${}^4T_{1b}$ but shifted to the low energies by the energy of the ${}^4T_2$ zero-phonon transition energy, and (2) by using, as in Ref. 14, the a_{1g} configuration curve model sketched in Figs. 6 and 7 and refined, as previously, by using the Struck and Fonger theory.

Similarly, Figs. 11 and 12 not only show the stimulated emission cross sections σ_e that we have calculated from the fluorescence spectra using McCumber's theory,[15] with the available ESA data in this infrared domain, but also the ESA band shapes that we can determine as above, by the first method and that we have noted σ_{01} (${}^4A_2 \rightarrow {}^4T_{1a}$). $\nu_{\text{laser}}^{\text{max}}$ gives the position of the oscillation frequency evidenced in the past.

In the case of MgF$_2$:V^{2+} the intensity of the ESA band σ_1 is adjusted so that the computed gain curve noted $\sigma'_e = \sigma_e - \sigma_1$ be maximum at the frequency $\nu = \nu_{\text{laser}}^{\text{max}}$. If the σ polarized band shape σ_{01} is used one obtains $\sigma_1 \simeq 0.25\sigma_{01}$, thus,

$$\sigma'_e \simeq \sigma_e - 0.25\sigma_{01} \ .$$

In the case of KMgF$_3$:V^{2+} the intensity of the band σ_1 is adjusted to the experimental ESA data and one obtains $\sigma_1 \simeq 0.15\sigma_{01}$, thus, in the emission domain,

$$\sigma'_e \simeq \sigma_e \ .$$

Surprisingly enough the shifted GSA bands labeled σ_{01} give the best agreements to the widths and the positions of the experimental ESA bands (see Figs. 9–14). As in the case of the Cr^{3+}-doped low-field systems the ESA features which can be deduced from a simple configuration curve model are far from being satisfactory. This disagreement is particularly important in the case of the ${}^4T_2 \rightarrow {}^4T_{1a}$ ESA transitions: the configuration curve model indicates absorption band shapes much narrower than the true ones.

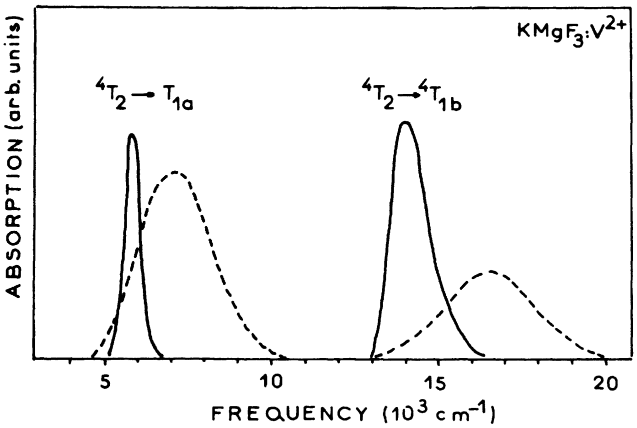

FIG. 13. ${}^4T_2 \rightarrow {}^4T_{1a}$ and ${}^4A_2 \rightarrow {}^4T_{1b}$ GSA spectra shifted by the energy of the ${}^4T_2$ zero-phonon transition energy (dashed line) and calculated ${}^4T_2 \rightarrow {}^4T_{1a}$ and ${}^4T_2 \rightarrow {}^4T_{1b}$ ESA spectra obtained by using the CC model and SF theory (solid line) (see text) in KMgF$_3$:V^{2+}.

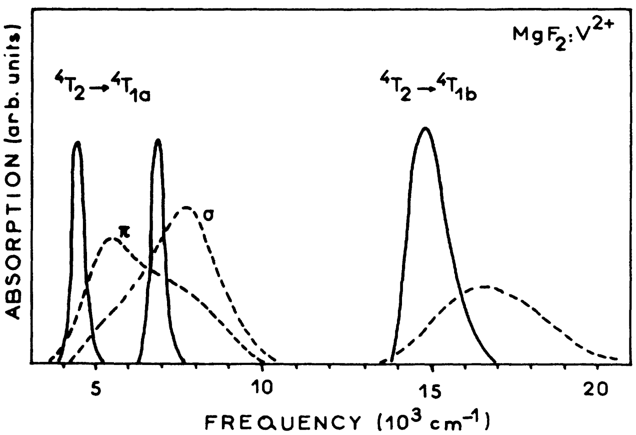

FIG. 14. ${}^4A_2 \rightarrow {}^4T_{1a}$ and ${}^4A_2 \rightarrow {}^4T_{1b}$ GSA spectra shifted by the energy of the ${}^4T_2$ zero-phonon transition energy (dashed line) and calculated ${}^4T_2 \rightarrow {}^4T_{1a}$ and ${}^4T_2 \rightarrow {}^4T_{1b}$ ESA spectra obtained by using the CC model and SF theory (solid line) (see the text) in MgF$_2$:V^{2+}.

As asserted before the true shape of the ESA bands is likely due to more than one interacting phonons. In other words the GSA and the ESA vibronic transitions may be associated to different modes.[16] It is possible, but it is hard to predict without a deeper study of the excited-state spectroscopy.

In the end, we can make the following concluding remarks. In the Cr^{3+} as well as in the V^{2+}-doped low-field systems (i) the a_{1g} single-mode configuration curve model gives a rather good overall description of the GSA bands but it is very approximative as to the ESA features. The GSA bands shifted by the zero-phonon energy of the absorbing excited state give a much better agreement to the latter. (ii) The cross sections of the ground-state and excited-state-absorption transitions $^4A_2 \rightarrow {}^4T_{1a}$ and $^4T_2 \rightarrow {}^4T_{1b}$, respectively, in the visible region have the same order of magnitude. (iii) The cross sections of the stimulated emission and excited-state-absorption transitions in the infrared also have the same order of magnitude, probably less than a factor of 3 difference. (iv) $KMgF_3:V^{2+}$ appears as an extraordinary good laser system since it could work at room temperature in a very interesting spectral domain (around 1.06 μm) without being affected by prohibitive ESA losses as in $MgF_2:V^{2+}$. Moreover, benefits can be drawn from the band displacements with temperature for obtaining a large laser tunability domain, likely going from 0.95 to 1.15 μm.

ACKNOWLEDGMENTS

We would like to thank first Dr. L. J. Andrews from GTE Laboratories, Inc., Waltham, MA, for having provided us with a sample of $GSGG:Cr^{3+}$. It allowed us to test our experimental setup in the visible, as well as in the infrared domains. We would also like to thank Drs. M. D. Shinn and W. Krupke from Lawrence Livermore National Laboratory (LLNL), Livermore, CA, very much for having provided us with the samples of $KMgF_3:V^{2+}$ and $MgF_2:V^{2+}$ used in our ESA experiments, and Dr. M. J. Weber for his help in the transaction. Part of this work was supported by the French Direction des Recherches et Etudes Techniques (DRET) Grant No. 84/071. The Laboratoire de Physico-Chimie des Matériaux Luminescents is "Unité Associée No. 442 du Centre National de la Recherche Scientifique" (France).

---

[1] L. F. Johnson and H. J. Guggenheim, J. Appl. Phys. **38**, 4837 (1967).
[2] P. F. Moulton, Workshop on Tunable Solid State Lasers, Fort Belvoir, Virginia, 1983 (unpublished).
[3] J. C. Walling, in *Proceedings of the Tunable Laser Conference II Zigzag, Oregon,* edited by A. B. Budgor, L. Esterowitz, and L. G. Deshazer (Springer-Verlag, Berlin, 1986), Vol. 52, p. 196.
[4] W. Knierim, A. Honold, V. Brauch, and V. Dürr, J. Opt. Soc. Am. **3**, 119 (1986).
[5] R. Moncorgé and T. Benyattou, following paper, Phys. Rev. B **37**, 9186 (1988).
[6] M. D. Sturge, F. R. Merritt, L. F. Johnson, H. J. Guggenheim, and J. P. Van Der Ziel, J. Chem. Phys. **54**, 405 (1971).
[7] M. D. Sturge, Phys. Rev. B **1**, 1005 (1970).
[8] M. D. Sturge, H. J. Guggenheim, and M. H. L. Pryce, Phys. Rev. B **2**, 2459 (1970).
[9] L. N. Fuerhelm and W. A. Sibley, J. Phys. C **16**, 799 (1983).
[10] M. V. Iverson, J. C. Windscheif, and W. A. Sibley, Appl. Phys. Lett. **36**, 183 (1980).
[11] C. W. Struck and W. H. Fonger, J. Lumin. **14**, 253 (1976).
[12] M. D. Sturge, Solid State Commun. **9**, 899 (1971), and references therein.
[13] L. J. Andrews, A. Lempicki, B. C. McCollum, J. C. Giunta, R. M. Bartram, and J. F. Dolan, Phys. Rev. B **34**, 2735 (1986).
[14] L. J. Andrews, S. M. Hitelman, M. Kokta, and D. Gabbe, J. Chem. Phys. **84**, 5229 (1986).
[15] D. E. McCumber, Phys. Rev. **134**, A299 (1964).
[16] L. J. Andrews, in *Proceedings of the Tunable Laser Conference II Zigzag, Oregon,* edited by A. B. Budgor, L. Esterowitz, and L. G. Deshazer (Springer-Verlag, Berlin, 1986), Vol. 52, p. 44.